

Supplementary Information

Nanometer-Thick Single-Crystalline Nanosheets Grown at the Water-Air Interface

Fei Wang,¹ Jung-Hun Seo,² Guangfu Luo,¹ Matthew B. Starr,¹ Zhaodong Li,¹ Dalong Geng,¹ Xin Yin,¹ Shaoyang Wang,¹ Douglas G. Fraser,¹ Dane Morgan,¹ Zhenqiang Ma,² Xudong Wang^{1,*}

1. Department of Material Science and Engineering, University of Wisconsin—Madison, Madison, Wisconsin 53706, United States

2. Department of Electrical and Computer Engineering, University of Wisconsin—Madison, Madison, Wisconsin 53706, United States

* Email: xudong@engr.wisc.edu

Table of Contents

1. Methods.....	2
2. Additional SEM images of ZnO nanosheets on Si substrate.	4
3. X-ray Photoelectron Spectroscopy (XPS) of ZnO nanosheets.	5
4. SEM images of ZnO nanosheets on holey carbon TEM grids.....	7
5. Control experiments using stearic acid as the surfactant monolayer.	8
6. Thickness measurements of ZnO nanosheets with 1.5X less dense oleylsulfate monolayer.	9
7. Synthesis of NiO and Au nanosheets by ionic layer epitaxy	10
8. Calculation of electric potential profile and Zn ²⁺ concentration profile from the surfactant-water interface into the bulk solution.....	12
9. Thickness measurements of ZnO nanosheets by AFM.....	15
10. DFT simulation methods and results on the crystal structure and band structure of ZnO nanosheets	16
References.....	19

1. Methods.

Synthesis

In a typical synthesis, 17 mL aqueous solution containing 25 mM $\text{Zn}(\text{NO}_3)_2$ and hexamethylenetetramine (HMT) was prepared in a glass vial. Subsequently, 10 μL chloroform solution containing 0.1 vol % sodium oleyl sulfate was spread on the water surface. This glass vial was then screw-capped and placed in a 60 $^\circ\text{C}$ convection oven. ZnO nanosheets would appear in about 1 hour 40 minutes and could be scooped using an arbitrary substrate for characterization and device fabrication.

Fabrication process of ZnO nanosheet-based FETs.

A 50 nm thick layer of Al_2O_3 by atomic layer deposition at 300 $^\circ\text{C}$ was first coated over a heavily doped Si substrate. A few 300 mesh Cu TEM grids (bar width of 10 μm) were then attached onto each substrate. These TEM grids were used as shadow masks and the substrate was coated with Cr/Au/Cr (5 nm/45 nm/5 nm) by e-beam evaporation. After removing the grids and thoroughly cleaning the substrates with isopropanol and acetone, the substrates were used to directly scoop the nanosheets from the surface of the reaction solution. Since the nanosheets were densely distributed on the water-air interface, some of them naturally sat between two hexagonal metal pads defined by TEM grids. These nanosheet-based FETs were then measured by probes without any further treatment. Figure S1A shows a metal pad array with nanosheets on them and Figure S1B shows the single nanosheet-based FET from which the I-V characteristics in main text Figure 4 were obtained.

The hole concentration and hole mobility were calculated by following two equations, respectively.

$$n_e = \frac{V_{th} \cdot C_{ox}}{q \cdot w \cdot L}, C_{ox} = \frac{A_{channel} \cdot \epsilon_0 \cdot \epsilon_{ox}}{t_{ox}}, \text{ and } \mu = \frac{L^2 \cdot g_m}{C_{ox} \cdot V_{ds}}$$

where V_{th} is the threshold voltage. C_{ox} is the capacitance of the dielectric oxide. Q is the charge of an electron. W , h , and L are the channel width, height, and length of the nanosheet, respectively. $A_{channel}$ is the channel area defined by the channel length times channel width. ϵ_0 and ϵ_{ox} are the electrical permittivity of vacuum and Al_2O_3 , respectively. The latter was assumed to be 10 based on literature value and the growth condition.^{1,2} t_{ox} is the thickness of Al_2O_3 . g_m is the transconductance at gate voltage V_{ds} .

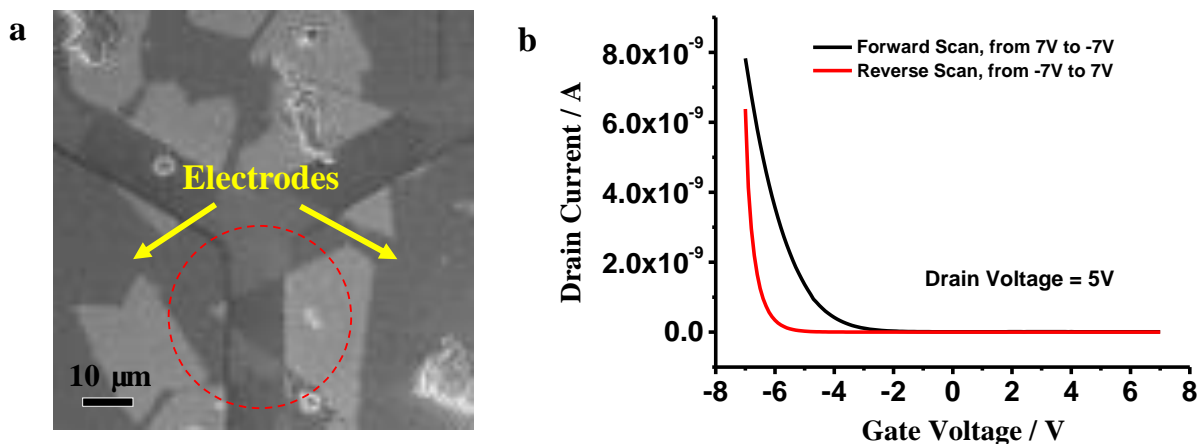


Figure S1. | Further information on ZnO nanosheet FET devices. **a.** SEM image of the device (red dash circled) whose I-V characteristics were shown in the main text Figure 4. The metal pad array was defined by a TEM grid with ZnO nanosheets transferred directly from the surface of synthesis solution. The substrate was highly-doped Si wafer coated with 50 nm Al₂O₃ by atomic layer deposition. Some of the nanosheets fell right between two metal pads and hence formed FET devices. **b.** Forward and reverse scan of drain current *versus* gate voltage of the FET.

2. Additional SEM images of ZnO nanosheets on Si substrate.

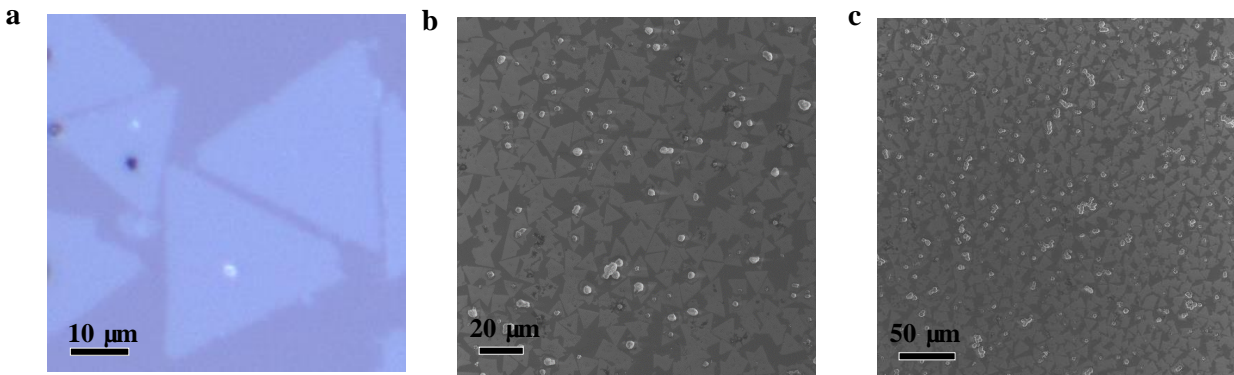


Figure S2. Additional of single-crystalline ZnO nanosheet triangles densely transferred to a SiO₂-coated Si substrate. a. Optical microscopy image, **b & c,** low magnification SEM images. The nanosheets show lighter contrast.

3. X-ray Photoelectron Spectroscopy (XPS) of ZnO nanosheets.

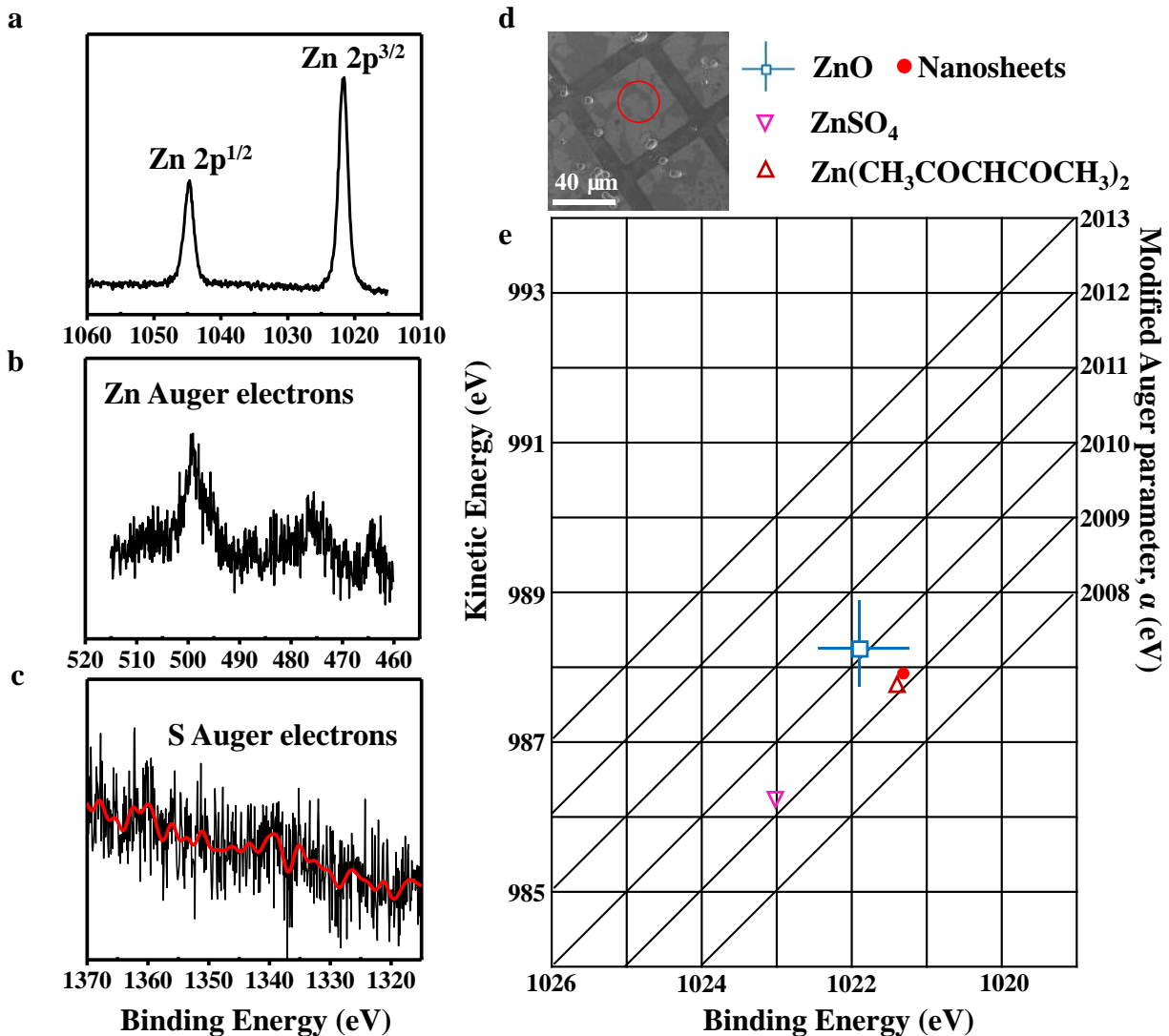


Figure S3. | XPS characterization of ZnO nanosheets. **a**, XPS spectrum of Zn. **b**, and **c**, Auger electron spectra of Zn and S, respectively. The red curve in **c** is a smoothed curve of the spectrum. **d**, SEM image of the nanosheet that was focused on to acquire the XPS spectra. **e**, Wagner plot of Zn based on the binding energy and kinetic energy of Zn.

XPS spectra of ZnO nanosheets were acquired by Thermo K-alpha X-ray photoelectron spectrometer with a focused, monochromatic X-ray source and monoatomic ion gun. Figure S3A, B, and C show the binding energy of Zn, and the Auger electron peaks of Zn and S respectively. The red curve in C was a smoothed version of the original spectrum. Figure 3D is an SEM image of the focused area. The nanosheet in focus was on a metal pad on a Si/Al₂O₃ substrate. Figure S3E is a Wagner plot showing the modified Auger parameter of Zn, which is the sum of the kinetic energy of the Auger transition and Zn 2p^{3/2} binding energy). From the plot we can see that the Zn²⁺ ions in ZnO nanosheets have the same modified Auger parameter as ZnSO₄. At the

same time, their position on the Wagner plot is very close to that of organic Zn compound. Therefore we can infer that there was specific bonding between Zn^{2+} ions in ZnO nanosheets and the sulfate group in oleylsulfate surfactant. The position of Zn^{2+} ions in the Wagner plot is also within the range of ZnO.

4. SEM images of ZnO nanosheets on holey carbon TEM grids.

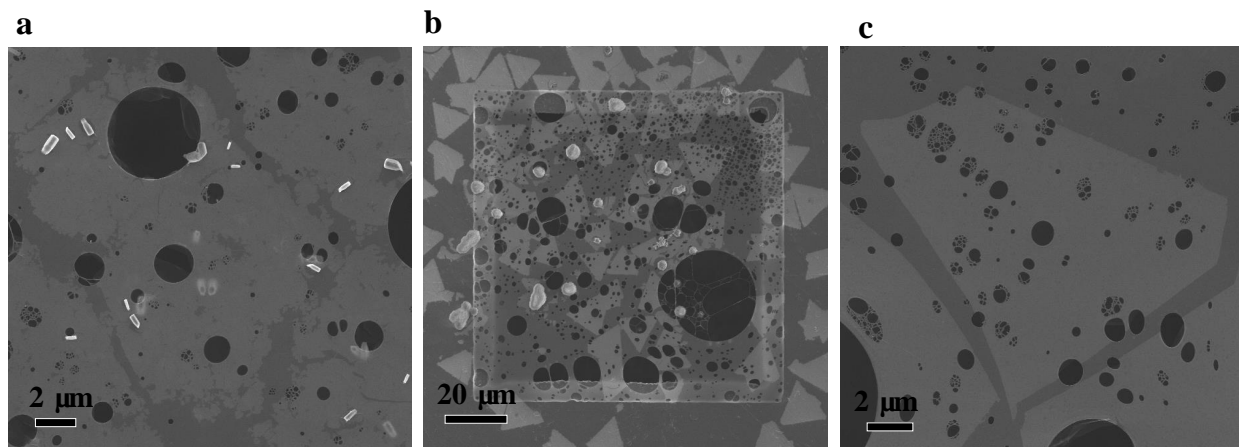


Figure S4. | SEM images of ZnO triangle nanosheets on a holey carbon film TEM grid. a, Polycrystalline nanosheets without faceted edges obtained at earlier stage of the reaction. **b, and c,** Low-magnification and zoomed-in images of single-crystalline ZnO triangle nanosheets, respectively.

5. Control experiments using stearic acid as the surfactant monolayer.

To further prove the critical role of the interactions between oleylsulfate and Zn^{2+} ions, we did the syntheses with the same experimental parameters except using stearic acid to replace oleylsulfate. As shown in Figure S5 below, we could only obtain large area amorphous film with sporadic, small crystallites, without forming faceted triangular morphology, much like the amorphous film formed initially during the synthesis using oleylsulfate. Therefore, it is certain that the interactions between oleylsulfate and Zn^{2+} ions are more than just electrostatic, and the specific bonding between the two parties is necessary to help the inter-distance between oleylsulfate molecules adapt to the Zn^{2+} ions in order to foster the epitaxial growth of ZnO nanosheets.

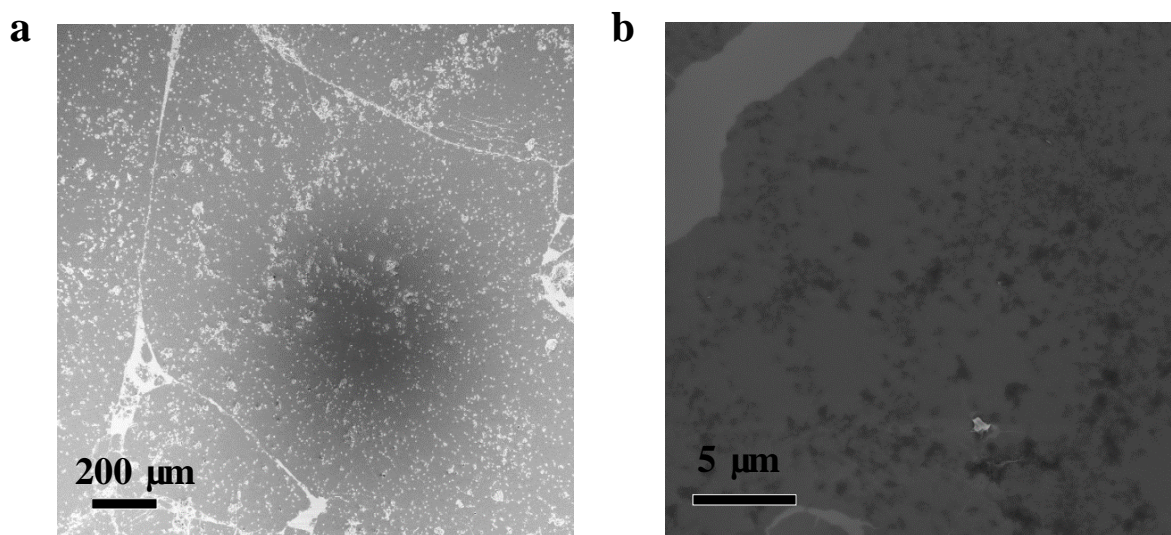


Figure S5. | SEM images of nanosheets obtained when stearic acid was used to form the surfactant monolayer. a, A low-magnification image showing their sizes up to millimeters. **b,** A zoomed-in image showing the non-faceted edges of these nanosheets.

6. Thickness measurements of ZnO nanosheets with 1.5X less dense oleylsulfate monolayer.

We also conducted experiments using 1.5X less dense oleylsulfate monolayer while keeping every other experiment parameters the same. Single-crystalline triangular ZnO nanosheets with similar size and thickness distribution were obtained (Figure S9a). The fact that single-crystalline ZnO nanosheets were grown under an oleylsulfate monolayer with different packing density further supports our idea of adaptive ionic layer epitaxy as a formation mechanism. If the formation follows the principles of conventional epitaxial growth, then there must be a stringent lattice match between the oleylsulfate monolayer and the ZnO nanosheets (0001) facet.

The thickness of the resulting nanosheets was measured by AFM to be 2.88 ± 0.41 nm and is plotted together with the calculated Zn^{2+} concentration profile as shown in Figure S9b. A good match between the Zn^{2+} concentrated zone and ZnO nanosheet thickness can be clearly identified. This observation further supports our argument that the Zn^{2+} concentrated zone under surfactant monolayer played a dominating role in determining the thickness of crystalline ZnO nanosheets.

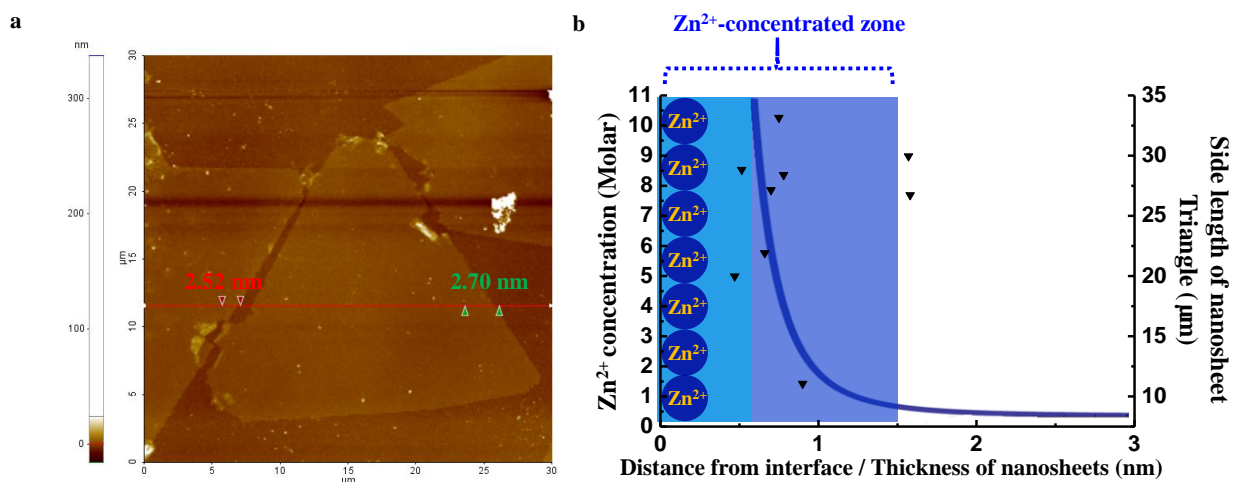


Figure S6 | Thickness of nanosheets when the density of oleylsulfate monolayer is 1.5X less. a. Thickness measurement of nanosheets by AFM. b, like in Figure 3 in the main text, the blue shaded band represents a positively charged stern layer primarily composed of Zn^{2+} ions. The blue curve plots the concentration of Zn^{2+} from the end of the Stern layer (blue shaded area within the first 0.6 nm) into the bulk solution. The black triangles mark the thickness of monocrystalline nanosheets measured by AFM. The right vertical axis is the side length of single-crystalline nanosheet triangles.

7. Synthesis of NiO and Au nanosheets by ionic layer epitaxy

In a typical synthesis of NiO nanosheets, 0.0648g NiCl₂ was dissolved in 50 mL DI water. After complete dissolution, 130 μ L hydrazine was added to the aqueous solution. Subsequently, 10 mM 1M NaOH solution was added, yielding a clear green solution. Depending on the opening size of the reactor, 0.02 mg/L chloroform solution of stearic acid was spread onto the surface of the growth solution. After 5 mins, the solution was placed in 70 $^{\circ}$ C oven and the reaction was conducted for 30 minutes.

To synthesis Au nanosheets, in a 6-dram vial, 10 μ L of a 0.10 M NaOH solution was diluted with 5.790mL of water and 1.000mL of a 2.0 mM L-Arginine solution. To this, 0.200mL of 17.14mM HAuCl₄ solution was added and gently swirled to combine. 10 μ L of stearic acid in chloroform (1mg/5mL) was gently dropped on top of the water and left to evaporate for 10 minutes. The vial was then capped tightly and placed in a 90 $^{\circ}$ C convection oven for 2 to 7 hours. The vial was left to cool to room temperature and the surface of the water was then sampled with a SiO₂-coated silicon wafer for SEM imaging.

Figure S6a shows an SEM image of the NiO hexagonal nanosheets. Similar to ZnO nanosheets, they are about 10 to 20 μ m in length on their edges. Figure S6b is a high-resolution TEM image taken from one of the hexagonal nanosheet. The TEM image reveals a single-crystalline rock salt structure of NiO and the exposed surface is (101). The inset is an electron diffraction pattern, in which the diffraction spots are indexed. Figure S6c is a topography scan of a hexagonal NiO nanosheet and its thickness is found to be 10 nm or below. X-ray photoelectron spectrum (Figure S8d) shows a Ni 2p peak where the binding energy is typically associated with Ni²⁺. Figure S6e is an SEM image of a corner of a sub-millimeter sized Au nanosheet. TEM characterization of this nanosheet (Figure S6f) shows a polycrystalline nature with 2-4 nm crystalline size. AFM topography scan shows a thickness of 4.4 nm, which indicates the Au nanosheet is a single layer of 2-D aggregation of Au nanoparticles. XPS spectrum reveals the spin-orbital split peaks of Au 4f that are associated with metal Au.

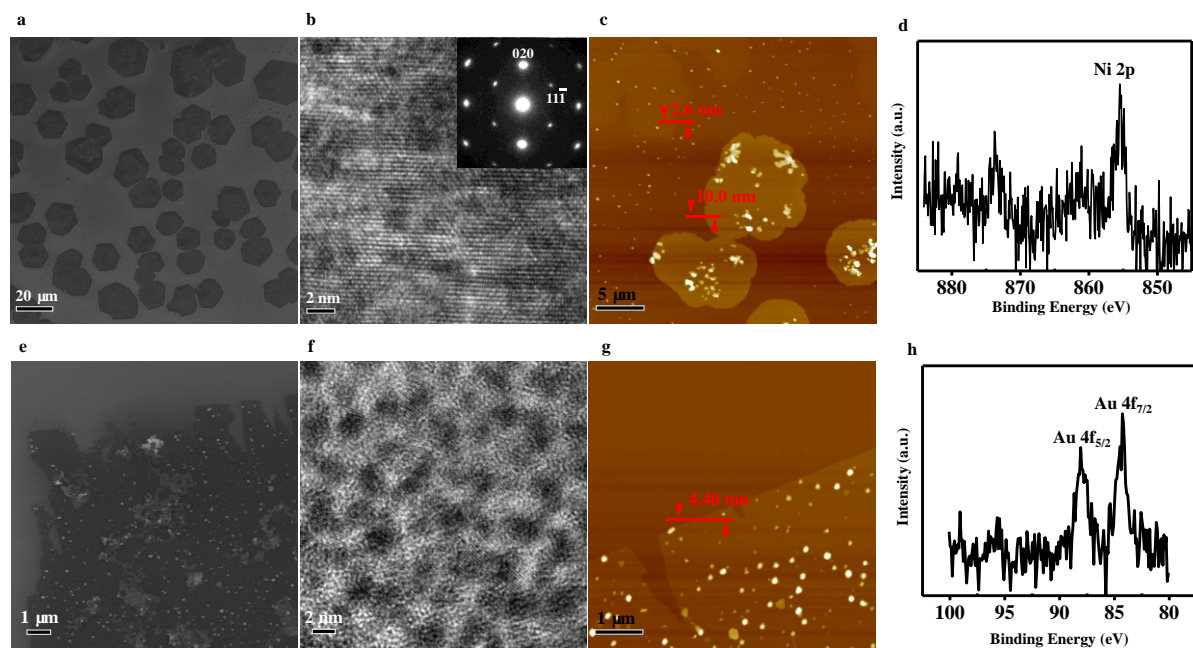


Figure S7. | Structural characterization of NiO and Au nanosheets **a** and **e**, SEM images of NiO and Au nanosheets, respectively, **b** and **f**, high-resolution TEM images of NiO and Au nanosheets, respectively, **c** and **g**, AFM topography scans of NiO nanosheets and a Au nanosheet. **d** and **h**, XPS spectra of NiO nanosheets and Au nanosheets revealing the +2 and 0 valence states of Ni and Au, respectively.

8. Calculation of electric potential profile and Zn^{2+} concentration profile from the surfactant-water interface into the bulk solution.

A charged surface, such as the surfactant monolayer, will push and pull on charged species in solution. The ions in solution will reorganize themselves about the charged surface, screening monolayer's influence on the bulk solution. The ratio of concentrations of species i in bulk solution (n_i^0) at bulk solution potential ($\phi^0 = 0$) to its concentration (n_i) found at any other potential (ϕ) is taken to depend upon the Boltzmann factor in the following way:

$$n_i = n_i^0 e^{\left(\frac{-z_i e \phi(x)}{kT}\right)} \quad (\text{S1})$$

where z_i is the charge of ion i , and e is the charge of the electron, ϕ is the potential relative to bulk solution, x is a measure of distance into solution and perpendicular to the monolayer surface, k is the Boltzmann constant, and T is absolute temperature. Under meager potentials, e.g. 1 Volt, and reasonable bulk ion concentrations, Eq. S1 will produce large, nonphysical ion concentrations (e.g. $n_i > \frac{1 \text{ Mole}}{\text{cm}^3}$). To determine whether 'large' potentials would be found in the studied system, Eq. S2 and S3 were used.³

$$\sigma^M = \epsilon \epsilon_0 \left(\frac{d\phi}{dx}\right)_{x=0} \quad (\text{S2})$$

$$\left(\frac{d\phi}{dx}\right) = \sqrt{\frac{2kT}{\epsilon \epsilon_0} \sum_i \left(n_i^0 \left[e^{\left(\frac{-z_i e \phi_{x=0}}{kT}\right)} - 1 \right] \right)} \quad (\text{S3})$$

where σ^M is the charge density of the monolayer, ϵ is the relative permittivity of the material (80 for water), ϵ_0 is the electrical permittivity of free space, $\left(\frac{d\phi}{dx}\right)_{x=0}$ is the potential gradient (electric field strength) at the monolayer's surface, and $\phi_{x=0}$ is the potential at the monolayer's surface. Taking σ^M as -0.801 C m^{-2} (i.e. $\frac{1 \text{ electron}}{20 \text{ \AA}^2}$) and solving for $\phi_{x=0}$, we indeed encountered large potentials that were capable of inducing large, nonphysical ion concentrations. Table S1 shows the type of ion concentrations expected from applying Eq. 2 directly to the experimental conditions we studied.

Table S1. | Parameters used and calculated concentrations of various ions from Eq. S2 assuming no physical size of ions.

Species i	n_i^0 ($\frac{\text{ions}}{\text{m}^3}$)	z_i	$\phi_{x=0}$ (V)	n_i ($\frac{\text{ions}}{\text{m}^3}$)
Zn^{2+}	1.12734×10^{25}	2	0.23309	1.27136×10^{32}
H^+	1.51269×10^{21}	1	0.23309	5.07991×10^{24}
OH^-	2.39746×10^{18}	-1	0.23309	7.13914×10^{14}
NO_3^-	2.93399×10^{25}	-1	0.23309	8.73681×10^{21}
NH_4^+	6.02063×10^{24}	1	0.23309	2.02184×10^{28}
ZnNO_3^+	7.70834×10^{23}	1	0.23309	1.27158×10^{27}

If we model the hydrated ions as hard spheres, then the maximum packing density possible is the close packing structure. Taking Zn^{2+} ions as an example, each with a hydration diameter (d) of 6 Å,⁴ then the maximum 3D packing density possible is given by:

$$\text{Maximum 3D Density} = \frac{\text{Zn}^{+2} \text{ ions}}{\text{Volume}} = \frac{\left(\frac{3}{2}\right)+3+\left(\frac{3}{2}\right)}{\frac{3\sqrt{3}}{2}a^2c} = \frac{6}{\frac{3\sqrt{3}}{2}d^2\left(2d\sqrt{\frac{2}{3}}\right)} = 6.54729 * 10^{27} \frac{\text{ions}}{\text{m}^3} \quad (\text{S4})$$

Thus, the total of all ion concentrations at the closest approach to the 2D charged layer must be equal to or less than this atomic density.

$$\sum n_i \leq 6.54729 * 10^{27} \frac{\text{ions}}{\text{m}^3} \quad (\text{S5})$$

Table S1 shows a clear violation of this condition.

Iterative numerical calculation was applied to find the limit of ϕ at which Eq. S2 and S3 obtained the condition required in Eq. S5. This yielding the critical criteria for the surface potential: $\phi_{x=0} \leq 0.090994$ V. In order to achieve this potential, far less than the 0.23309 V previously determined to be present at the charged monolayer, a charged stern layer is assumed to form adjacent to the charged self-assembled surfactant monolayer. Using Eq. S2 and S3 again, except now fixing $\phi_{x=0} = 0.090994$ V and solving for σ , it is found that a surface charge density of $0.0651358 \frac{\text{C}}{\text{m}^2}$ is capable of maintaining a $\phi_{x=0} = 0.090994$ V in the required aqueous conditions. Physically, this apparent surface charge density σ^A is the 2D charge density necessary to create an electric field strong enough to condense the charged species in solution into a close packing structure. Because the superposition principle applies in electromagnetism, the 2D charge density (σ^A) that the solution experiences is a sum of the surfactant monolayer's charge density (σ^M) and the Stern layer's charge density (σ^S).

$$\sigma^A = \sigma^M + \sigma^S \quad (\text{S6})$$

To gain insight into the nature of the charged Stern layer, and determine if it is physical reasonable, rearranging Eq. 7 and solving for σ^S yields:

$$\sigma^S = \sigma^A - \sigma^M = (-0.0651358) - (-0.801) = 0.735952 \frac{\text{C}}{\text{m}^2} \quad (\text{S7})$$

This value for σ^S is well within the theoretical maximum 2D charge density (σ_{Max}^S) obtained by modeling the Stern layer as a 2D array of charged Zn^{+2} ions (Fig. S6).

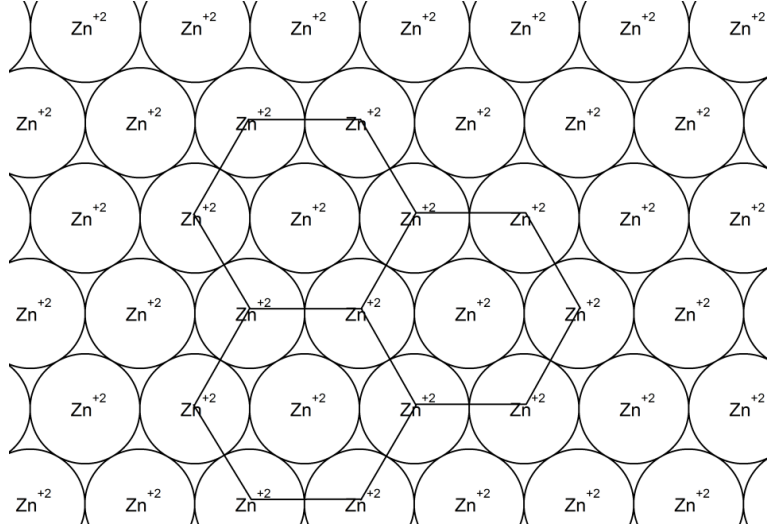


Figure S8. | A 2D array of Zn^{2+} ions used to calculate the theoretical maximum 2D charge density, $\sigma_{\text{Max}}^{\text{S}}$, in order to check the charge density we obtained from Eq. S7 is physically possible.

The following is used to calculate $\sigma_{\text{Max}}^{\text{S}}$:

$$\sigma_{\text{Max}}^{\text{S}} = \frac{\text{Charge}}{\text{Area}} = \frac{\left(\frac{\text{Zn}^{+2} \text{ ions}}{\text{hexagon}}\right) \times \left(\frac{\text{Charge}}{\text{Zn}^{+2} \text{ ion}}\right)}{\frac{3\sqrt{3}}{2}d} = \frac{\left(6\left(\frac{1}{3}\right)+1\right) \times (2 \cdot e)}{\frac{3\sqrt{3}}{2}(d)} = 1.0278 \frac{\text{C}}{\text{m}^2} \quad (\text{S8})$$

$\sigma_{\text{Max}}^{\text{S}}$ is greater than the previously determined value of $0.735952 \frac{\text{C}}{\text{m}^2}$ for σ^{S} and thus σ^{S} is deemed a physically reasonable value for the stern layer charge density.

9. Thickness measurements of ZnO nanosheets by AFM.

We measured the edge length (size) and the thickness of a number of randomly selected nanosheets transferred to a Si substrate from the same batch. Typical thickness measurement of the triangle nanosheets was done at their edges and shown in Figure 1D in the main text. Figure S7 shows a typical thickness measurement of amorphous nanosheets at the cracks within them.

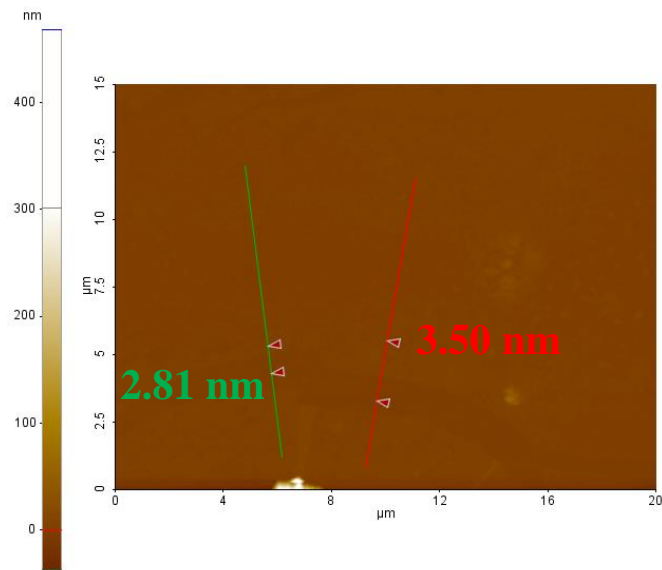


Figure S9. | AFM topography scans to obtain the statistical measurement of the thickness of amorphous nanosheets. There were cracks in the millimeter-sized amorphous films from which thickness measurements can be done by topography scans.

10. DFT simulation methods and results on the crystal structure and band structure of ZnO nanosheets

We performed density functional theory calculations with the Vienna *ab initio* simulation package.^{5,6} The Perdew–Burke–Ernzerhof (PBE) exchange-correlation functional was employed except the band structure calculations. The projector augmented wave method was used together with the following potentials: H_GW ($1s^1$, $E_{\text{cut}} = 300.0$ eV), C_GW_new ($2s^22p^2$, $E_{\text{cut}} = 414.0$ eV), O_s_GW ($2s^22p^4$, $E_{\text{cut}} = 334.7$ eV), S_GW ($3s^23p^4$, $E_{\text{cut}} = 258.7$ eV), and Zn_pv_GW ($3d^{10}4s^2$, $E_{\text{cut}} = 360.2$ eV). The plane-wave energy cutoff was set to 500 eV. The ZnO(0001) slab consists of a 2×2 supercell ($\sim 6.5 \text{ \AA} \times 6.5 \text{ \AA}$) in plane and five bulk ZnO atomic layers ($\sim 10 \text{ \AA}$) together with a $\sim 10 \text{ \AA}$ of vacuum layer out of plane. The Brillouin zone is sampled with a $5 \times 5 \times 1$ Monkhorst-Pack grid. The atom positions and in-plane lattices are fully relaxed until the force on each is less than 10^{-3} eV/\AA . The surfactant molecules are packed closely on the slab surface, with a density of one surfactant molecule per four surface Zn atoms. To reduce the computational cost, a 3-carbon chain is used to represent the 18-carbon chain in oleylsulfate. Tests show that this simplification has a minor influence to the properties we are interested in.

For the bare ZnO(0001) slab, we surprisingly find that the most stable atomic arrangement is the tetragonal structure. In contrast, the planar structure is 44 meV per Zn atom (44 meV/Zn) higher than the tetragonal one. Although a bilayer planar ZnO(0001) was experimentally obtained on Ag(111),⁷ our calculations suggest that the planar slab is more stable than the tetragonal one only when the thickness is equal to or less than three ZnO layers (Fig. S11). The wurtzite structure is the least stable form and it dynamically evolves to the planar structure in a fully geometry relaxation, which may explain the previous theoretical findings of planar structures.⁸ For a ZnO(0001) slab with surfactants closely packed on one surface, the tetragonal structure is still the most stable one. The wurtzite-like structure is less stable than the tetragonal structure by 10 meV/Zn, while the planar structure becomes dynamically unstable. The energetics of the three phases are summarized in Table SII.

Table SII. | Summary of the total energies (meV/Zn) of the three phases. Values of the tetragonal structures are set to zero.

	Wurtzite	Planar	Tetragonal
Bare ZnO(001) slab	unstable	44	0
Zn(0001) slab with surfactant	10	unstable	0

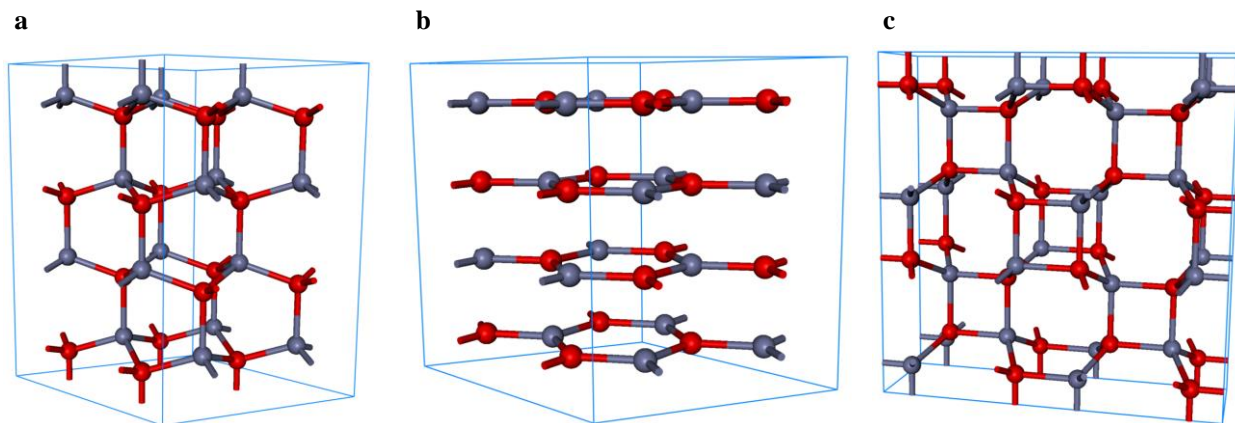


Figure S10. | Crystal structures of **a**, Hexagonal Wurtzite ZnO, **b**, Planar ZnO, and **c**, tetragonal ZnO.

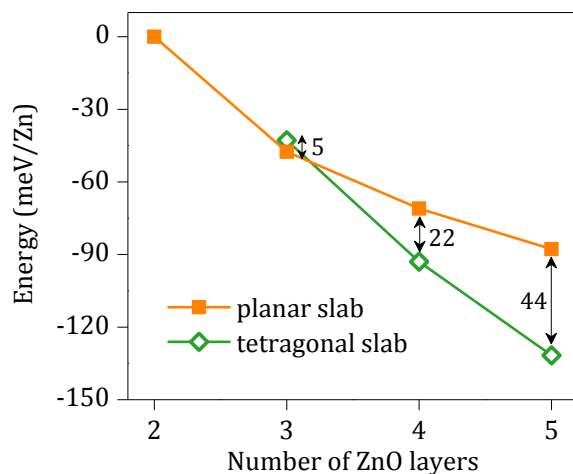


Figure S11. | Total energy of bare planar and tetragonal Zn(0001) slabs with different thickness. The value of a 2-layer planar slab is set to zero. The 2-layer tetragonal slab is unstable and evolves to the planar structure during geometry optimization.

JEMS was used to simulate the electron diffraction patterns along the surface normal of the nanosheets for Wurtzite structure (0001) and the tetragonal structure (100).

Wurtzite (0001)

Tetragonal (100)

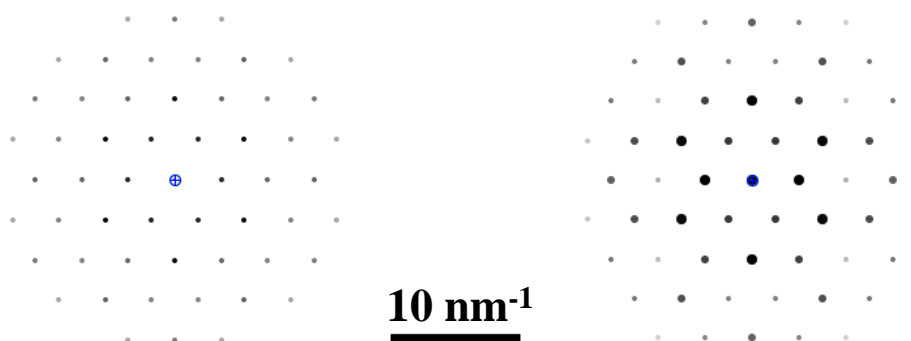


Figure S12. | Simulated electron diffraction pattern along the surface normal of the nanosheets. **Left**, Hexagonal Wurtzite structure when the surface normal is along the c -axis of the lattice. **Right**, Tetragonal structure ($P4_2/MNM$) when the surface normal is along the a -axis of the lattice. The two diffraction patterns overlap with each other.

References

- 1 Tanner, C. M., Perng, Y. C., Frewin, C., Sadow, S. E. & Chang, J. P. Electrical performance of Al_2O_3 gate dielectric films deposited by atomic layer deposition on 4H-SiC. *Appl. Phys. Lett.* **91** (2007).
- 2 Yota, J., Shen, H. & Ramanathan, R. Characterization of atomic layer deposition HfO_2 , Al_2O_3 , and plasma-enhanced chemical vapor deposition Si_3N_4 as metal-insulator-metal capacitor dielectric for GaAs HBT technology. *J. Vac. Sci. Technol., A* **31**, 01A134 (2013).
- 3 Bard, A. J. & Faulkner, L. R. *Electrochemical Methods: Fundamentals and Applications*. (Wiley, 2000).
- 4 Persson, I. Hydrated metal ions in aqueous solution: How regular are their structures? *Pure Appl. Chem.* **82**, 1901-1917 (2010).
- 5 Kresse, G. & Furthmuller, J. Efficiency of ab-initio total energy calculations for metals and semiconductors using a plane-wave basis set. *Comp Mater Sci* **6**, 15-50 (1996).
- 6 Kresse, G. & Furthmuller, J. Efficient iterative schemes for ab initio total-energy calculations using a plane-wave basis set. *Phys. Rev. B* **54**, 11169-11186 (1996).
- 7 Tusche, C., Meyerheim, H. L. & Kirschner, J. Observation of depolarized ZnO(0001) monolayers: Formation of unreconstructed planar sheets. *Phys. Rev. Lett.* **99** (2007).
- 8 Freeman, C. L., Claeysens, F., Allan, N. L. & Harding, J. H. Graphitic nanofilms as precursors to wurtzite films: Theory. *Phys. Rev. Lett.* **96** (2006).